Materials Science & Engineering A 651 (2016) 55–62

Contents lists available at ScienceDirect

Materials Science & Engineering A

journal homepage: www.elsevier.com/locate/msea

Investigation of thermal aging effects on the tensile properties of Alloy 617 by *in-situ* synchrotron wide-angle X-ray scattering

Xiang Liu [a,*], Kun Mo [b], Yinbin Miao [a,b], Kuan-Che Lan [a], Guangming Zhang [c], Wei-Ying Chen [a,b], Carolyn Tomchik [a], Rachel Seibert [d], Jeff Terry [d], James F. Stubbins [a,e]

[a] Department of Nuclear, Plasma, and Radiological Engineering, University of Illinois at Urbana-Champaign, 216 Talbot Laboratory, 104 South Wright Street, Urbana, IL 61801, USA
[b] Nuclear Engineering Division, Argonne National Laboratory, Lemont, IL 60439, USA
[c] School of Materials Science and Engineering, University of Science and Technology Beijing, Beijing 10083, China
[d] College of Science, Illinois Institute of Technology, Chicago, IL 60616, USA
[e] International Institute for Carbon Neutral Energy Research (WPI-I2CNER), Kyushu University, 744 Motooka, Nishi-ku, Fukuoka 819-0395, Japan

ARTICLE INFO

Article history:
Received 10 June 2015
Received in revised form
21 October 2015
Accepted 25 October 2015
Available online 27 October 2015

Keywords:
Alloy 617
High-temperature thermal aging
Wide-angle X-ray scattering
$M_{23}C_6$ carbide

ABSTRACT

The nickel-base Alloy 617 has been considered as the lead candidate structural material for the intermediate heat exchanger (IHX) of the Very-High-Temperature Reactor (VHTR). In order to assess the long-term performance of Alloy 617, thermal aging experiments up to 10,000 h in duration were performed at 1000 °C. Subsequently, *in-situ* synchrotron wide-angle X-ray scattering (WAXS) tensile tests were carried out at ambient temperature. $M_{23}C_6$ carbides were identified as the primary precipitates, while a smaller amount of M_6C was also observed. The aging effects were quantified in several aspects: (1) macroscopic tensile properties, (2) volume fraction of the $M_{23}C_6$ phase, (3) the lattice strain evolution of both the matrix and the $M_{23}C_6$ precipitates, and (4) the dislocation density evolution during plastic deformation. The property–microstructure relationship is described with a focus on the evolution of the $M_{23}C_6$ phase. For aging up to 3000 h, the yield strength (YS) and ultimate tensile strength (UTS) showed little variation, with average values being 454 MPa and 787 MPa, respectively. At 10,000 h, the YS and UTS reduced to 380 MPa and 720 MPa, respectively. The reduction in YS and UTS is mainly due to the coarsening of the $M_{23}C_6$ precipitates. After long term aging, the volume fraction of the $M_{23}C_6$ phase reached a plateau and its maximum internal stress was reduced, implying that under large internal stresses the carbides were more susceptible to fracture or decohesion from the matrix. Finally, the calculated dislocation densities were in good agreement with transmission electron microscopy (TEM) measurements. The square roots of the dislocation densities and the true stresses displayed typical linear behavior and no significant change was observed in the alloys in different aging conditions.

1. Introduction

The Very-High-Temperature Reactor (VHTR) is a leading candidate of the Gen-IV advanced reactors as proposed by the Next Generation Nuclear Plant (NGNP) program [1,2]. The VHTR is designed as a high-efficiency system with capabilities of providing process heat and coupling to hydrogen production facilities. The net plant efficiency of the VHTR can exceed 50% at 1000 °C, much greater than the 33% efficiency of current light water reactors. However, the high temperature environment poses challenges for reactor structural materials, especially when combined with high pressures and an aggressive atmosphere [3]. In particular, since the design lifetime of the VHTR is 60 years, high-temperature and long-term thermal-aging can induce significant degradation in the mechanical properties of the structural materials, and may pose potential challenges for long-term reactor operation.

One of the key components in the VHTR system is the intermediate heat exchanger (IHX), which is responsible for the heat transfer from the primary system to secondary systems [4,5]. The IHX is designed to function in an impure helium environment at temperatures up to 950 °C, and pressures around 7 MPa. Recently, Alloy 617, a solid-solution strengthened, nickel–chromium–cobalt–molybdenum alloy, has been selected as the structural materials for the IHX [6]. This alloy was developed in the 1970s for high-temperature applications such as gas turbines, combustion cans, ducting, and structural components for power-generating plants [7]. Numerous studies on Alloy 617 have been performed to investigate creep properties, tensile behavior at various

* Corresponding author. Fax: +1 217 333 2906.
E-mail address: xliu128@illinois.edu (X. Liu).

http://dx.doi.org/10.1016/j.msea.2015.10.098
0921-5093/

temperatures, corrosion resistance, and thermal aging effects [8–22]. In 1974, Mankins et al. studied the aging effects on the microstructure and phase stability of Alloy 617 at 649–1093 °C and identified $M_{23}C_6$ as the main stable precipitates at all temperatures and a small amount of gamma prime ($L1_2$-structured Ni_3Al) at 760 °C [9]. The aging study of Alloy 617 was extended to 8000 h in the temperature range of 593–816 °C by Kimball et al., and $M_{23}C_6$ carbides precipitating at grain boundaries were again reported [11]. Later in 1980, Kihara et al. studied the creep properties at 1000 °C and discussed the microstructural development, especially the evolution of $M_{23}C_6$ precipitates during creep, and proposed the existence of the Ostwald ripening mechanism under loading [12]. Recently, Mo et al. studied the aging effects at 900 °C and 1000 °C up to 3000 h, using electron microscopy techniques to provide detailed information on the size distribution, morphology, and coherency of $M_{23}C_6$ precipitates [13–15]. Ren et al. have reviewed the aging effects on Alloy 617, and summarized most of the previous works and important experimental data [16,17].

In previous studies, $M_{23}C_6$ has been identified as the major precipitate during high-temperature thermal aging, and has been considered the main reason for changes in strength/hardness of Alloy 617 [13]. The size, volume fraction, and location of the precipitates are dependent on the thermal aging conditions. To better understand their behavior and interaction mechanism with the metallic matrix during mechanical loading in different aging conditions, we conducted *in-situ* tensile tests combined with synchrotron wide-angle X-ray scattering (WAXS) to characterize the microstructural changes during loading. The experiments are based on long-term (up to 10,000 h) thermal aging experiments on Alloy 617 at 1000 °C [14,15,22]. From the high-energy X-ray measurements, both the macroscopic tensile behavior and the microstructural evolution involving the change in volume fraction of the carbide phase, the lattice strain development for both carbides and metallic phases, and dislocation densities during loading were determined.

2. Description of experiments

The Alloy 617 was provided by Haynes International, Inc. in plate form. The one-inch thick plate has a nominal composition of Ni–22.1Cr–12.2Co–9.46Mo–1.104Fe–0.39Ti–1.03Al–0.064Mn–0.08C–0.05Si–0.017Cu, in wt%. The alloy was hot worked and solution treated at 1177 °C for 37 min. The heat number was 861758808 [13]. In order to study the thermal aging of Alloy 617 for applications in the IHX component of VHTR, the aging experiments were performed in laboratory air conditions at 1000 °C, which was above the gamma prime solvus [9]. The alloy was aged to 10, 30, 100, 300, 1000, 3000, and 10,000 h so that the aging effects could be systematically characterized. Miniature tensile specimens were then machined from the aged alloys. The effects of aging on tensile behavior were investigated by performing *in-situ* tensile tests and WAXS at room temperature. The experiments were carried out at the 10-ID-B beamline at the Advanced Photon Source (APS), Argonne National Laboratory (ANL).

The synchrotron WAXS experimental setup is shown in Fig. 1. The tensile tests were performed with a Deben 5 kN dual lead-screw tensile stage. The *mar*345 image plate X-ray detector was used to measure X-ray diffraction patterns. The energy of the incident X-ray beam was 50 keV (λ=0.2480 Å). The dimensions of the miniature tensile specimens were 1.19 mm × 0.75 mm × 5.00 mm (width × thickness × gauge length). Uniaxial tensile tests were performed in the displacement control mode, with a displacement step of 0.02 mm in the elastic region and 0.05–0.10 mm in the plastic region. After each displacement, the position was kept constant during each X-ray exposure. The speed

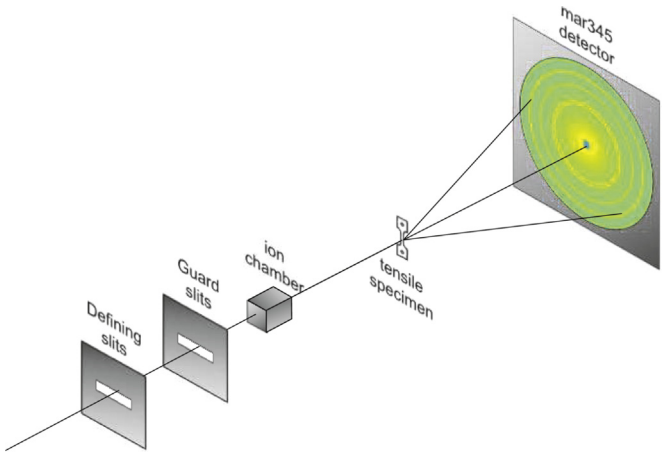

Fig. 1. Schematics of *in-situ* synchrotron X-ray diffraction experiment setup. The energy of incident X-ray beam was 50 keV. A *mar*345 image plate detector was used for X-ray detection.

range of the gearbox was in the range of 20 μm/min to 1.5 mm/min, and the highest strain rate was estimated to be around 0.005/s, which was slightly higher than conventional tensile tests that use a strain rate of 10^{-4}/s to 10^{-3}/s. Nonetheless, the tensile data can be compared with existing data that employed different strain rates, since Alloy 617 has been known to be insensitive to strain rate at ambient temperature [23,24]. In order to cover more grains during each exposure to reduce statistical errors, the X-ray beam size was chosen to be 700 μm × 700 μm, and the total diffraction volume of around 0.3675 mm^3 was attained. The X-ray exposure time ranged from 2 s in the elastic region to about 30 s near fracture so as to maximize the signal-to-noise ratio without saturation. Load and displacement data were recorded to determine the macroscopic stress–strain curves. Due to limited beam time, only one sample was tested for each aging time point. *Ex-situ* tensile measurements were carried out independently to determine the uncertainty in the applied stress, which is estimated to be less than 2%.

In order to validate the WAXS results, transmission electron microscopy (TEM) was used to characterize the $M_{23}C_6$ carbides and measure the dislocation densities in the alloy that was aged for 10,000 h. Both pre-tensile and post-tensile miniature samples were examined. TEM specimens were lifted out from the gauge part of the mechanically polished miniature samples using an FEI HELIOS 600i FIB. Bright field (BF) images were used to measure the average dislocation density. Selected area diffraction (SAD) was used to characterize the $M_{23}C_6$ carbides. All the TEM images were taken using a JEOL 2010 LaB_6 TEM operated at 200 kV.

3. Results and discussion

3.1. Macroscopic tensile properties during aging

Macroscopic tensile data are shown in Fig. 2. Fig. 2(a) shows the engineering stress–strain curves for both the as-received and aged specimens. The yield strength (YS) and the ultimate tensile strength (UTS) are shown in Fig. 2(b). Compared to the alloy in the as-received condition, the YS and UTS of the alloy aged for t=10 h increased by 35 MPa and 22 MPa, respectively. However, for the samples aged for 10 h up to 3000 h, only slightly variations in both the YS and UTS have been observed. In the 10–3000 h regime, the average YS and UTS are 450 MPa and 790 MPa, respectively. For the samples aged for 10,000 h, the YS and UTS decreased to 380 MPa and 720 MPa, respectively. This shows that the long-term

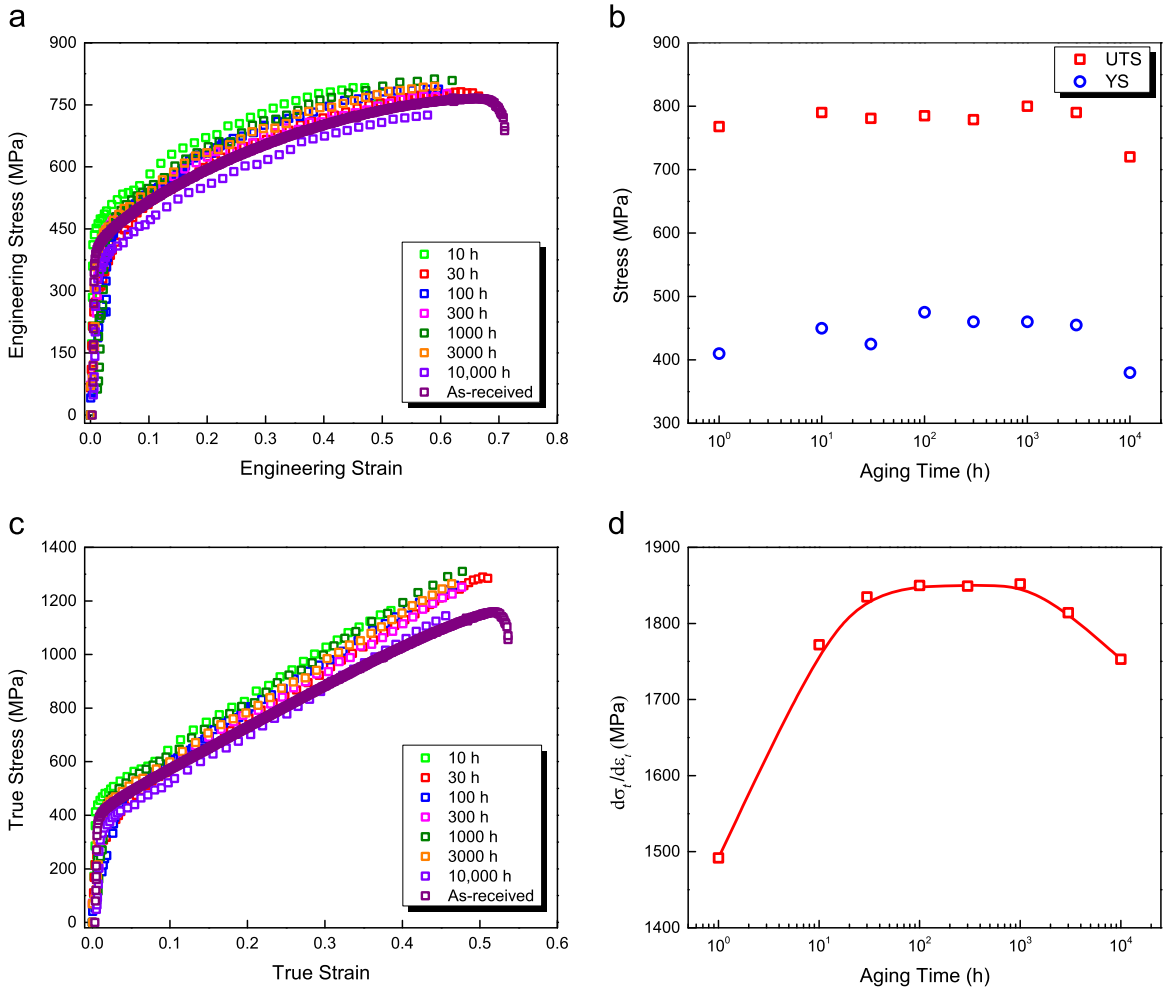

Fig. 2. Macroscopic tensile data for Alloy 617 at different aging times: (a) engineering stress *vs* engineering strain; (b) YS and UTS; (c) true stress *vs* true strain; and (d) strain hardening rate $d\sigma_t/d\varepsilon_t$. (The as-received condition is arbitrarily placed at $t = 10^0$ h in the logarithmic coordinate.)

thermal aging (about 10,000 h at 1000 °C) caused considerable degradation in the tensile properties of Alloy 617.

The true stress and the true strain are calculated from the engineering stress and engineering strain by $\sigma_t = \sigma_e(1 + \varepsilon_t)$ and $\varepsilon_t = \ln(1 + \varepsilon_e)$, respectively. Fig. 2(c) and (d) shows the true stress–strain curves and the strain hardening rate $d\sigma_t/d\varepsilon_t$ for different aging times, respectively. The strain hardening rate reveals the hardening mechanism evolution during aging. Previous works have identified that two main mechanisms are related to the thermal aging process – short-term hardening due to carbide precipitation and long-term softening due to Ostwald ripening of carbides [12,14]. The ripening effect is related to the coarsening of $M_{23}C_6$ precipitates that reach a certain constant volume fraction after long-term aging. As a result, the average distance between $M_{23}C_6$ precipitates increases, and the strengthening due to the Orowan bowing mechanism decreases. Our results show that for thermal aging at 1000 °C, short-term hardening occurs around 10 h. The plateau of the strain hardening rate between 100 h and 1000 h indicates that the coarsening is not significant in this time scale (otherwise the strain hardening rate would have dropped). For long-term aging, the strain hardening rate begins to decrease at around 3000 h, which should be regarded as over-aged. At 10,000 h, there is an appreciable decrease in the strain hardening rate, indicating that the ripening effect becomes dominant. Quantitatively speaking, from plastic deformation theory, the flow stress is given by [25,26]

$$\tau \simeq \tau_y + \alpha Gb\sqrt{\rho} = \tau_{PN} + Gb/(L - 2r) + K/\sqrt{d} + \alpha Gb\sqrt{\rho}, \quad (1)$$

where G is the shear modulus, b is the Burgers vector of the dislocations, $L - 2r$ is the effective distance between obstacles, d is the average grain size, ρ is the dislocation density, and α is a correction factor (~0.2 for FCC systems). On the right-hand side of Eq. (1), the first term is the Peierls–Nabarro stress that accounts for lattice resistance; the second term describes the strengthening due to Orowan bowing; the third term represents the strengthening due to grain size and follows the Hall–Petch relation; and the last term is the strain hardening. The YS is determined by the sum of the first three terms. For Alloy 617, previous studies have shown that the grain structure and grain size did not undergo significant changes during thermal aging, primarily due to Zener pinning [14,23]. Therefore, it is reasonable to assume that the Peierls–Nabarro stress and the grain size strengthening terms ($\tau_{PN} + K/\sqrt{d}$) are the same for different aging times. Then, $\Delta\tau_y \simeq \Delta\tau_{Orowan}$. Since $\tau_{Orowan} \simeq Gb/(L - 2r)$, the change in the Orowan bowing stress is due to the change in the effective distance between precipitates. $M_{23}C_6$ precipitates exist in both intergranular and intragranular forms [23]. The size of the intergranular carbides is on the order of 0.5–2 μm and the intragranular carbides are on the order of 10–100 nm. Therefore, the stress needed for dislocation looping around intergranular precipitates is much lower than that for intragranular fine precipitates, and hence the latter is the dominant contribution to the Orowan bowing strength. After long-term aging, the ripening of

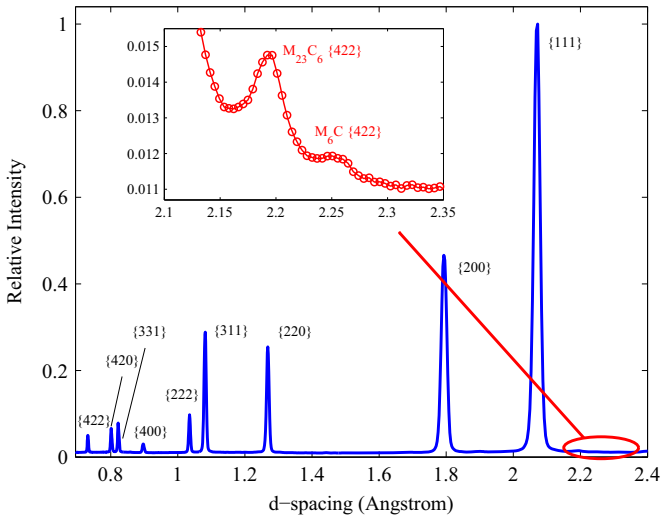

Fig. 3. The *d*-spacing plot of Alloy 617 at $t=10{,}000$ h showing {422} reflections from the $M_{23}C_6$ and M_6C phases. Major reflections from the face-centered cubic (FCC) matrix have also been indexed.

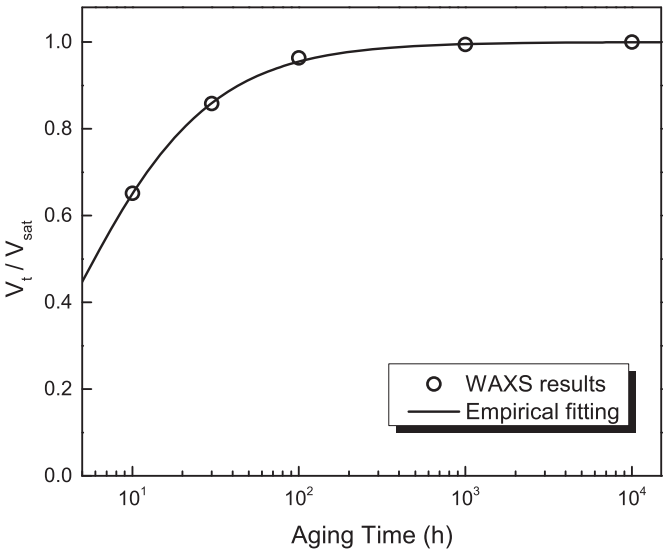

Fig. 4. Volume fraction of the $M_{23}C_6$ phase at different aging times.

intergranular carbides will reduce the number density of intragranular carbides, and the coarsening of intragranular carbides will further increase the effective distance, thus reducing the Orowan bowing stress. This leads to the conclusion that at 1000 °C, the YS of Alloy 617 increases by $M_{23}C_6$ precipitation during short-term aging, while the YS decreases by $M_{23}C_6$ precipitate coarsening during long-term aging.

3.2. Aging effects on carbide volume fraction and load partitioning

Due to the high energy and high intensity of synchrotron X-ray, the minor phases in metals and alloys, which can be hardly observed using lab-based X-ray machines, can be characterized with better resolved resolution. In Alloy 617, the WAXS results show that $M_{23}C_6$ is the main type of precipitates, though M_6C is also observed in much smaller amounts. Fig. 3 shows the relative intensity distribution as a function of *d*-spacing. The {422} reflections from both $M_{23}C_6$ and M_6C are identified. The amount of M_6C is so small that in some conditions it could not be clearly identified. Since $M_{23}C_6$ is the major type of precipitates, whose coarsening is directly related to the aging effect, the following analysis will focus on this type of precipitate.

For many alloys, one of the most important microstructural modifications induced by thermal aging is the precipitation and coarsening of the inclusion phases, which might also be the major strengthening phases. The change in size distribution and volume fraction of these strengthening phases will influence the tensile properties in several respects. For Alloy 617 aged at 1000 °C, the tensile properties are mainly affected by the $M_{23}C_6$ precipitates. Also, the rate of $M_{23}C_6$ precipitate nucleation and growth is strongly temperature dependent, the process is much faster at high temperatures (*e.g.* 1000 °C). As a result, the volume fraction of carbides increases at the early stage of aging, and a plateau may occur after aging to a certain time.

The volume fraction of the $M_{23}C_6$ phase is determined from the integrated intensities of WAXS diffraction peaks. For a material that contains *k* phases, the volume fraction of the *i*th phase can be obtained from X-ray diffraction (XRD) by [27–29]

$$V_i = \frac{\frac{1}{n_i}\sum_{j=1}^{n_i} I_i^j / R_i^j}{\sum_k \frac{1}{n_k}\sum_{j=1}^{n_k} I_k^j / R_k^j} \tag{2}$$

where *I* is the integrated intensity and *R* is the material scattering factor. The index *j* runs for all resolved reflections. For (*hkl*) plane, *R* is given by

$$R_{hkl} = \frac{1}{V^2}[|F_{hkl}|^2 p\left(\frac{1+\cos^2 2\theta}{\sin^2\theta\cos\theta}\right)]e^{-2M}, \tag{3}$$

where *V* is the volume of the unit cell; θ is the Bragg angle of the (*hkl*) plane; F_{hkl}, *p*, and e^{-2M} are the material scattering factor, the multiplicity factor, and the temperature factor, respectively.

Fig. 4 shows the normalized volume fraction (volume fraction divided by the saturation value, V_{sat}) of $M_{23}C_6$ carbides as a function of the aging time. The WAXS results were obtained using the integrated intensities. Due to the overlapping of the $M_{23}C_6$ peaks and the matrix peaks, only the 422 peak of the $M_{23}C_6$ carbides was used and the uncertainty is relatively large (around 25%) for phase fraction calculations. As can be seen, at 1000 °C most carbide precipitation happened around 10–30 h, and the volume fraction reaches a plateau after 100 h of thermal aging. This time scale is very consistent with the observed short-term hardening in Fig. 2, indicating that the $M_{23}C_6$ carbide precipitation is responsible for the observed short-term hardening for thermal aging at 1000 °C.

Besides the change in volume fraction, the size distribution of the $M_{23}C_6$ carbides is also strongly influenced by thermal aging. In Alloy 617, most intergranular $M_{23}C_6$ precipitates are irregular in shape that can be roughly described by the length and width. After long-term aging, the length of a $M_{23}C_6$ carbide can be as large as 2–3 μm and the width can be ~1 μm. Fig. 5 shows the TEM image of an incoherent intergranular carbide in a post-tensile specimen that has been aged for 10,000 h. The change in size distribution is due to the coarsening process, which was well characterized by Mo using scanning electron microscopy (SEM) [23].

Compared with the macroscopic tensile results, the rise in volume fraction of $M_{23}C_6$ carbides provides a good explanation of the short-term hardening which occurs around 10–30 h, as shown in Fig. 2(d). The minor variation in YS and UTS during 100–3000 h, shown in Fig. 2(b), is also validated by the plateau of the volume fraction during the same period. It is also noted that at 10,000 h, although the volume fraction remained the same, the YS, UTS, and

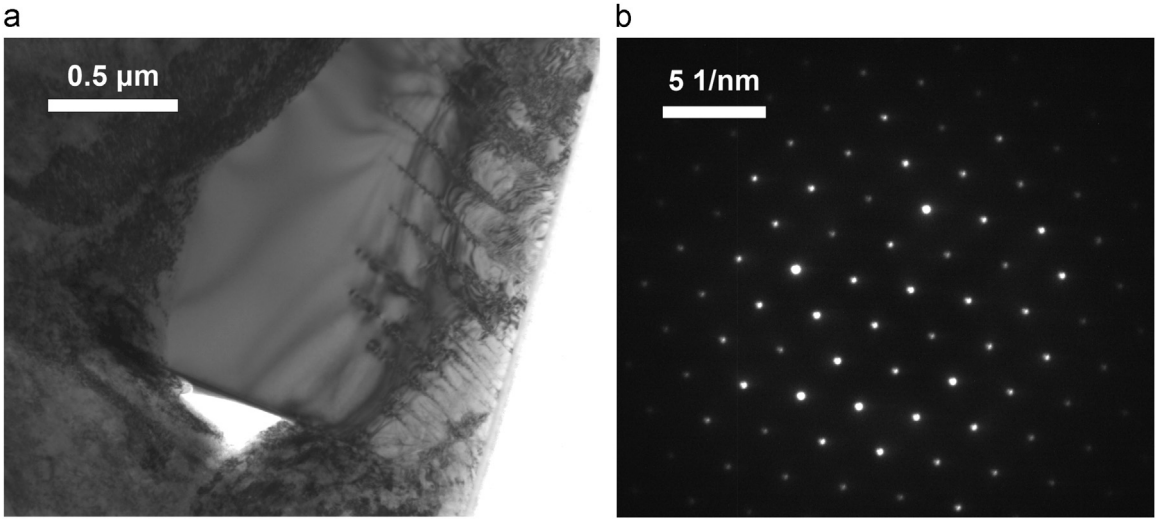

Fig. 5. (a) TEM bright field image of an intergranular $M_{23}C_6$ carbide and (b) the diffraction pattern, zone axis=[011].

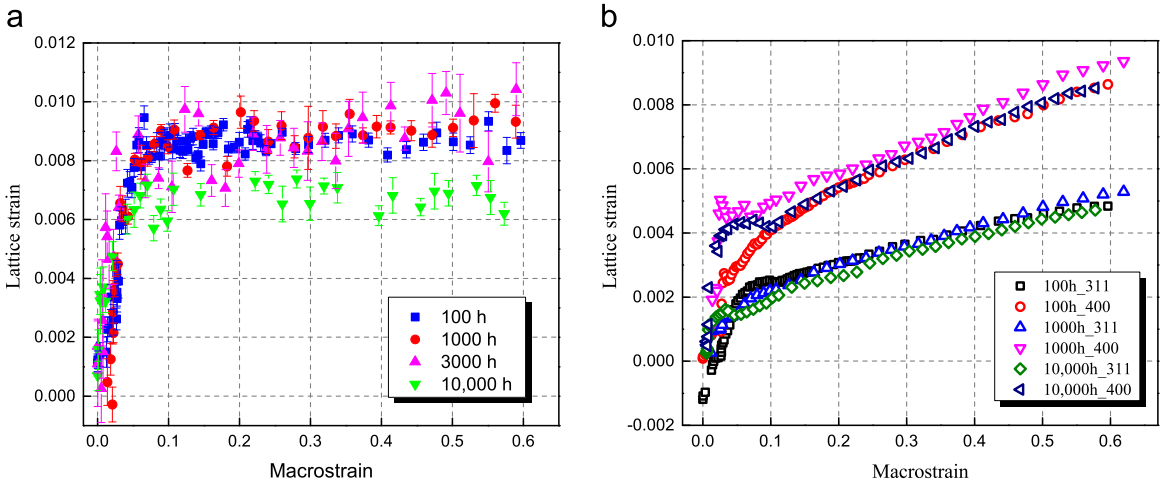

Fig. 6. Lattice strain evolution during the tensile loading: (a) the lattice strains of the $M_{23}C_6$ precipitate {422} reflection *vs* the macrostrain, and (b) the lattice strains of the metallic matrix {311} and {400} reflections *vs* the macrostrain, for Alloy 617 aged at 1000 °C to different times.

the strain hardening rate decreased. This loss of strength is due to the coarsening of $M_{23}C_6$ carbide particles since no further increase in the volume fraction of the carbides was observed for the 10,000-h case.

From the variation of a Debye–Scherrer ring during loading, the change in the corresponding *d*-spacing d^{hkl} can be determined. The lattice strain ε^{hkl} is obtained by $\varepsilon^{hkl} = (d^{hkl} - d_0^{hkl})/d_0^{hkl}$, where d_0^{hkl} is the reference *d*-spacing before tensile loading [28,30,31]. Although multiple reflections of $M_{23}C_6$ were observed, only {422} and {440} reflections were not overlapped with the reflections of the matrix. Since the intensity of the {422} reflection is higher, it was employed for analyzing the lattice strains of $M_{23}C_6$. Fig. 6(a) shows the lattice strain of $M_{23}C_6$ as a function of the macrostrain for Alloy 617 aged for 100, 1000, 3000, and 10,000 h at 1000 °C. Similarly in all these conditions, the lattice strain evolution of $M_{23}C_6$ can be divided into two regions: (1) at first, the lattice strain of $M_{23}C_6$ increases almost linearly with the macrostrain, and (2) after reaching a certain critical value in the early stage of sample yielding, the lattice strain of $M_{23}C_6$ maintains a constant level during the entire plastic deformation regime. A reasonable explanation involves consideration of the tensile fracture mechanism. During plastic deformation, geometrically necessary dislocations (GNDs) are generated to accommodate the inherent strain incompatibility between the $M_{23}C_6$ inclusions and the matrix [25]. Therefore, the internal stress is the result of both the applied stress and the stress caused by GNDs, *i.e.* $\sigma_T = \sigma_{Te} + \sigma_{GND}$ [25]. As the plastic strain increases, both σ_{Te} and σ_{GND} will increase. At certain critical strain values, nucleation of microcracks or microvoids occurs, leading to the fracture or decohesion of the $M_{23}C_6$ particles. The $M_{23}C_6$ precipitates exist in both intragranular and intergranular forms, with the intergranular particles having larger size (typically on the order of 0.5–2 μm). Therefore, intergranular coarse $M_{23}C_6$ precipitates are more susceptible to fracture or decohesion from the matrix. Fig. 5 shows a sub-micron void nucleated and coalesced at the carbide-matrix interface, leading to decohesion of the $M_{23}C_6$ precipitate.

For Alloy 617, it was found that the maximum lattice strains of the $M_{23}C_6$ particles were around 0.87% for aging up to 3000 h, though this value decreased to 0.68% for aging to 10,000 h. The decrease in the maximum lattice strain of $M_{23}C_6$ actually indicates a decrease in the maximum internal stress portioned to the $M_{23}C_6$ due to the coarsening of the $M_{23}C_6$ inclusions.

Lattice strain measures the elastic deformation component in both elastic and plastic regimes. For FCC materials, it is known that the bulk lattice strain can be approximated by the {311} reflection [23]. Fig. 6 shows the comparison of lattice strains of the matrix at different aging times. The {311} reflection is shown to represent the bulk lattice strain evolution, and the {400} reflection is shown

for comparison. It can be seen that the lattice strains from both {311} and {400} reflections have similar behaviors for all three cases, indicating that thermal aging up to 10,000 h has negligible effects on the elastic deformation component and the loading behavior of the host matrix. However, it is also noted that although there is little difference in the lattice strain evolution, the maximum lattice strains of both {311} and {400} reflections differ from each other. For t = 100, 1000, and 10,000 h, the maximum {311} lattice strains of the matrix are 0.484%, 0.529%, and 0.471%, and the corresponding maximum macrostrains are 59.6%, 62.0%, and 57.8%, respectively. The elongation to failure of specimens in as-received condition is 70.9%. Since the properties of the matrix were not significantly affected by thermal aging, it is clear that for aged specimens (especially the t=10,000 h case), fracture occurred before the matrix reaches the maximum possible internal stress. This indicates that the ductility of Alloy 617 is influenced by the $M_{23}C_6$ precipitates. Compared to as-received specimens, the elongation to failure reduced to 59.6% at t=100 h, due to the short-term hardening by carbide precipitation, as shown in Fig. 4. Subsequently, carbide coarsening leads to softening and the elongation to failure increased to 62.0% at t=1000 h. Accelerated coarsening happened after 1000 h and the size of carbides increased noticeably. At t=10,000 h, the maximum lattice strain of carbides reduced as a result of coarsening, leading to earlier fracture by void nucleation and coalescence, and the elongation to failure reduced to 57.8%.

Finally, it is worth mentioning that the lattice strain data in the elastic region is not as ideal as that obtained in the plastic regime due to the spotty X-ray diffraction rings as a result of the texture after hot-rolling of the alloy and its large grains after annealing. In the plastic deformation regime, subgrain structure begins to form along with a significant increase in dislocation density, thus the 2D diffraction rings become more continuous and uniform.

3.3. Aging effects on dislocation density evolution

Plastic deformation is directly related to the dislocation density evolution. Based on the aforementioned strain strengthening model, the flow stress is related to the total dislocation density by $\tau \simeq \tau_0 + \alpha G b\sqrt{\rho}$. The evolution of dislocation densities was obtained by analyzing the diffraction peak broadening in the full width at half maximum (FWHM) of the matrix using the modified Williamson–Hall (W–H) model [32,33]. In the modified W–H model, the broadening of diffraction peaks (after subtracting the instrumental broadening) is attributed to both crystalline size and dislocations. The governing equation is

$$\Delta K \simeq 0.9/D + (\pi M^2 b^2/2)^{1/2}\rho^{1/2}KC^{1/2} + O(K^2C), \quad (4)$$

where ΔK is related to the broadening by $\Delta K = 2\cos\theta\Delta\theta/\lambda$ (where θ is the diffraction angle and λ is the incident X-ray wavelength). On the right-hand side of Eq. (4), the first term represents the contribution of crystalline size, where D is the average crystalline size. The second term represents the contribution of dislocations, where $K = 2\sin\theta/\lambda$, M is a constant related to the cutoff radius of the dislocations, b is the Burgers vector, and C is the average dislocation contrast factor. In cubic systems, the contrast factor is determined by $\bar{C} = \bar{C}_{h00}(1 - qH^2)$, where $\bar{C}_{h00}$ is the average contrast factor of $h00$ reflections and H^2 is a fourth order invariant given by $(h^2k^2 + h^2l^2 + k^2l^2)/(h^2 + k^2 + l^2)^2$.

The values of $\bar{C}_{h00}$ and q are material dependent, and are different for screw and edge dislocations. As a first order approximation, the elastic constants of nickel (C_{11} = 249 GPa, C_{12} = 155 GPa, and C_{44} = 114 GPa) were used to estimate the dislocation contrast factor of Alloy 617 [34]. For screw dislocations, $\bar{C}_{h00}$ = 0.261 and q=2.209; for edge dislocations, $\bar{C}_{h00}$ = 0.265 and q=1.382. For simplicity, M=1 was used for the dislocation density calculation.

Fig. 7(a) shows the dislocation density evolution during plastic deformation, calculated from the WAXS data. The error bars were calculated from the uncertainties of curve fitting and are first order estimates of the deviation of the 1D line profile from ideal pseudo-Vigot functions. As can be seen, the alloy aged for 10,000 h presents the lowest values of dislocation density during the entire plastic regime. This can be explained by the long-term softening due to the ripening effect. In the later stage of plastic deformation, the dislocation density of the alloy aged for 1000 h is the highest among all samples. The alloy aged for 100 h attained the highest dislocation density during early stage of plastic deformation up to the strain of 20%, but increases slower upon further straining. Fig. 7(b) shows the linear relationship between the true stress σ_t and the square root of the dislocation density $\sqrt{\rho}$. The overall trend of dislocation development during tensile deformation, *i.e.* the dependence between flow stress and dislocation density, is similar for the samples in all aged conditions. This indicates that the dislocation multiplication and storage process is not significantly affected by thermal aging. However, there are some difference between t=100 h and the other two cases, as indicated by the linear fitting lines. The slope of the t=100 h one is apparently higher, which is due to short-term hardening resulted from the smallest $M_{23}C_6$ precipitates in all conditions.

In addition, TEM images were used to measure the dislocation densities in both pre-tensile and post-tensile Alloy 617 specimens

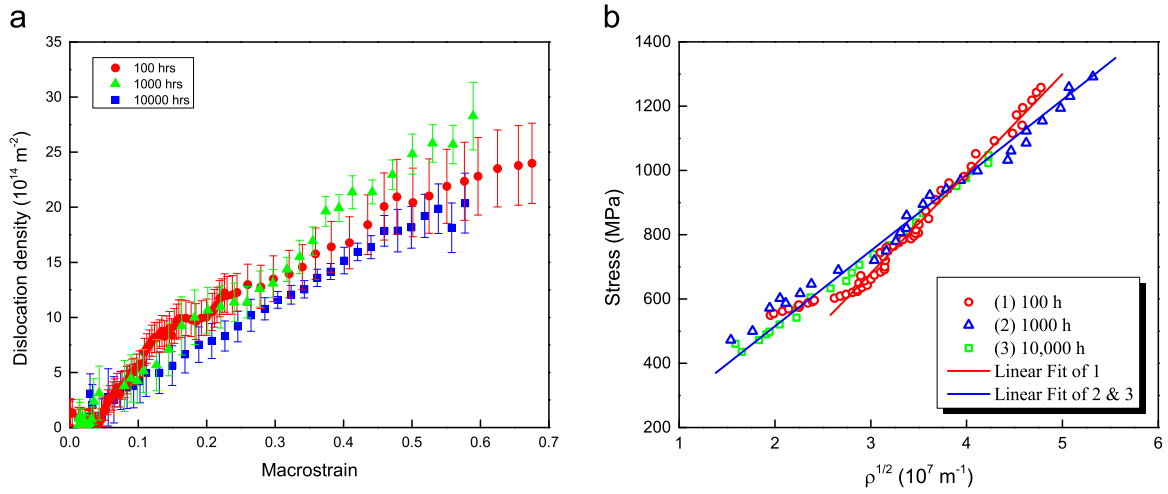

Fig. 7. Dislocation density evolution at different aging times: (a) dislocation density ρ *vs* the macrostrain and (b) $\sqrt{\rho}$ *vs* true stress σ_t.

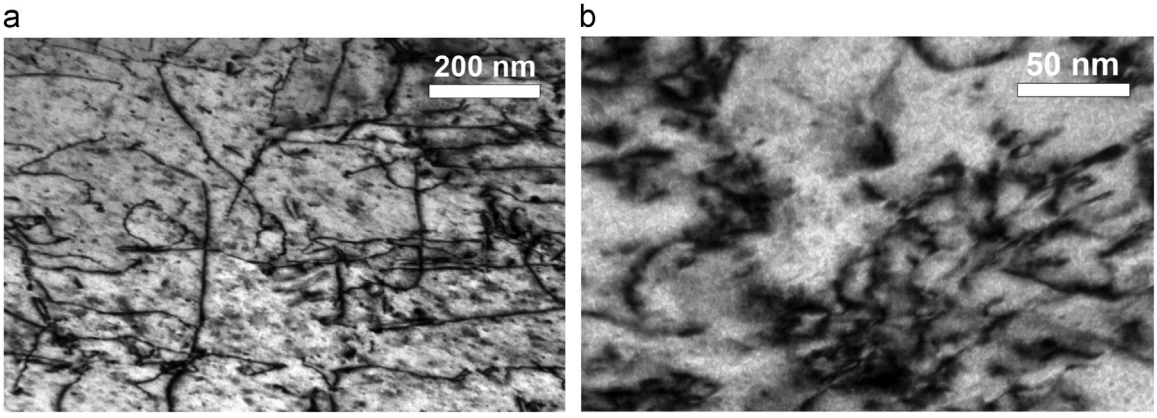

Fig. 8. TEM bright field images of (a) a pre-tensile specimen and (b) a post-tensile specimen. Both specimens were aged for 10,000 h at 1000 °C.

that were aged for 10,000 h. The average dislocation densities of the pre-tensile and post-tensile specimens shown in Fig. 8(a) and (b) are $2.3 \times 10^{14}\,m^{-2}$ and $1.6 \times 10^{15}\,m^{-2}$, respectively. From the WAXS data of the 10,000 h specimen, the dislocation densities in the elastic region and at failure are $2.1 \times 10^{14}\,m^{-2}$ and $2.0 \times 10^{15}\,m^{-2}$, respectively. Therefore, the dislocation densities from WAXS data and TEM results are in good agreement.

Besides the dislocation evolution during plastic deformation, twinning also plays an important role in Alloy 617. Fig. 9 shows several nano-twins found in a post-tensile specimen that had been aged for 10,000 h. Nano-twins were also found in specimens at different aging conditions. It is worth noticing that nano-twins showed grain-to-grain variation and in some grains they were not observed. Due to the aforementioned spotty diffraction rings and the heterogeneous spatial distribution of nano-twins, aging effect on the evolution of nano-twins during plastic deformation was not quantified.

4. Conclusion

This work is focused on the aging effects on Alloy 617 at 1000 °C, a relevant temperature for VHTR applications. In order to cover short-term aging and the over-aged regime, Alloy 617 samples were aged to 10, 30, 100, 300, 1000, 3000, and 10,000 h. The *in-situ* synchrotron X-ray diffraction technique was employed in combination with uniaxial tensile tests. All measurements were performed at room temperature. Based on the experimental results, the following conclusions can be drawn:

The overall effects of aging on the tensile behavior of Alloy 617 included a typical short-term hardening and a long-term softening. When compared to the as-received samples, the YS and UTS were increased by 35 MPa and 22 MPa, respectively, for $t=10$ h. From $t=30$ h to $t=3000$ h, there was little variation in the YS and UTS. For $t=10{,}000$ h, the YS and UTS were reduced to 380 MPa and 720 MPa, respectively.

Based on the synchrotron XRD, the main precipitates were identified as $M_{23}C_6$, though M_6C particles were also identified in a smaller amount. The aging temperature was above the gamma prime solvus and no gamma prime was observed. The volume fraction of $M_{23}C_6$ carbides was calculated using the integrated peak intensities and the size of $M_{23}C_6$ carbides was measured using TEM. It is found that the increase in volume fraction at 10–30 h is responsible for the short-term hardening and the increase in average size results in long-term softening.

The lattice strains of the $M_{23}C_6$ precipitates and the matrix showed distinct behaviors. After the elastic region, the lattice strain of $M_{23}C_6$ reaches a certain constant level and the lattice strain of the matrix increases linearly. This region of constant lattice strain of the $M_{23}C_6$ particles is due to microcrack growth or microvoid formation at large internal stresses. It was also found that the maximum lattice strain of $M_{23}C_6$ for aging up to 3000 h is around 0.87%, a value that reduces to 0.68% for aging to 10,000 h. This indicates the reduction in the maximum stress affordable by the $M_{23}C_6$ particles due to the coarsening process.

The dislocation density evolution at 100, 1000, and 10,000 h was calculated for comparison. It was found that in the $\sqrt{\rho}$ *vs* σ_t plot, the general trend was similar, indicating that the strain hardening behavior of Alloy 617 during aging was not significantly altered. However, the final dislocation density of $t=10{,}000$ h is apparently the lowest and the percent elongation at failure is also the smallest. This is well explained by earlier failure due to the reduction in the maximum affordable stress of $M_{23}C_6$ particles.

Finally, nano-twins were observed in some grains in post-tensile Alloy 617 specimens. The role of nano-twins on the plasticity of Alloy 617 and aging effects on twinning deformation need to be investigated in future work.

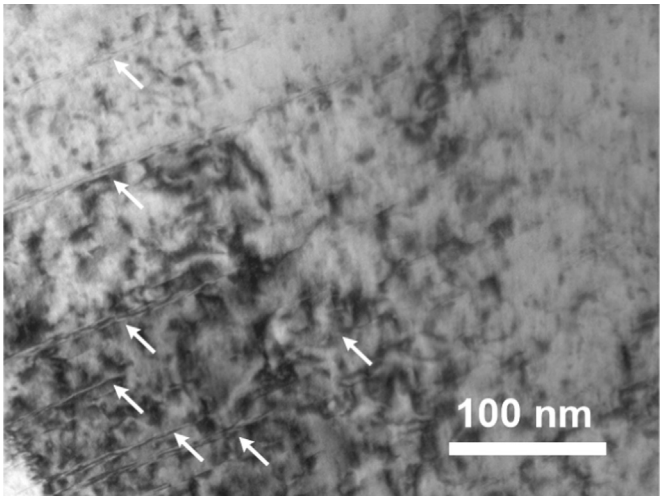

Fig. 9. TEM bright field image showing nano-twins formed in a post-tensile Alloy 617 specimen, which has been aged for 10,000 h.

Acknowledgments

The authors are grateful to Dr. Jonathan Almer for his WAXS analysis code. This work was supported by the U.S. Department of Energy, Office of Nuclear Energy under DOE Idaho Operations Office Contract DE-AC07-051D14517 as part of a Nuclear Science

User Facilities experiment. This work was also supported by the U. S. Department of Energy under Grants DE-FC07-07ID14819 and DOE NEUP 09-516. The authors also want to acknowledge the support of the International Institute for Carbon Neutral Energy Research (WPI-I2CNER), sponsored by the World Premier International Research Center Initiative (WPI), MEXT, Japan. Alloy 617 was provided by Haynes International, inc. The FIB and TEM experiments were carried out in the Frederick Seitz Materials Research Laboratory Central Facilities, University of Illinois. MRCAT operations are supported by the Department of Energy and the MRCAT member institutions. This research used resources of the Advanced Photon Source, a U.S. Department of Energy Office of Science User Facility operated for the DOE Office of Science by Argonne National Laboratory under Contract no. DE-AC02-06CH11357.

References

[1] D. Butler, Nature 429 (2004) 238–240.
[2] F. Southworth, P. Macdonald, D. Harrell, C. Park, E. Shaber, M. Holbrook, D. Petti, The Next Generation Nuclear Plant (NGNP) Project, Technical Report No. INEEL/CON-03-01150, Idaho National Laboratory (INL), 2003.
[3] P. Yvon, F. Carré, J. Nucl. Mater. 385 (2009) 217–222.
[4] C.H. Oh, E.S. Kim, M. Patterson, J. Eng. Gas Turbines Power 132 (2010) 032903.
[5] E. Kim, C. Oh, S. Sherman, Nucl. Eng. Des. 238 (2008) 2635–2647.
[6] W.R.N. Wright, J.K., T.-L. Sham, Next Generation Nuclear Plant Steam Generator and Intermediate Heat Exchanger Materials Research and Development Plan, Technical Report PLN-2084, Idaho National Laboratory, 2010.
[7] J. Hosier, D. Tillack, Metals Eng. Q. 12 (1972) 51–55.
[8] H. Kirchhöfer, F. Schubert, H. Nickel, Nucl. Technol. 66 (1984) 139–148.
[9] W. Mankins, J. Hosier, T. Bassford, Metall. Trans. 5 (1974) 2579–2590.
[10] H.W.S.P. Schneider, K.B. Ilschner, Nucl. Technol. 66 (1984) 289–295.
[11] O. Kimball, G. Lai, G. Reynolds, Metall. Mater. Trans. A 7 (1976) 1951–1952.
[12] S. Kihara, J.B. Newkirk, A. Ohtomo, Y. Saiga, Metall. Trans. A 11 (1980) 1019–1031.
[13] K. Mo, H.-M. Tung, J. Almer, M. Li, X. Chen, W. Chen, J.B. Hansen, J.F. Stubbins, J. Press. Vessel Technol. 135 (2013) 021502.
[14] K. Mo, G. Lovicu, H.-M. Tung, X. Chen, J.F. Stubbins, in: ASME 2010 Pressure Vessels and Piping Division/K-PVP Conference, American Society of Mechanical Engineers, Bellevue, Washington, USA, pp. 891–900.
[15] K. Mo, G. Lovicu, H.-M. Tung, X. Chen, J.F. Stubbins, J. Eng. Gas Turbines Power 133 (2011) 052908.
[16] W. Ren, R. Swindeman, J. Press. Vessel Technol. 131 (2009) 024002.
[17] W. Ren, R. Swindeman, J. Press. Vessel Technol. 131 (2009) 044002.
[18] L. Tan, X. Ren, K. Sridharan, T. Allen, Corros. Sci. 50 (2008) 3056–3062.
[19] R.N. Wright, Summary of Studies of Aging and Environmental Effects on Inconel 617 and Haynes 230, Technical Report, Idaho National Laboratory (United States), Funding organisation: DOE-NE (United States), 2006.
[20] S. Chomette, J.-M. Gentzbittel, B. Viguier, J. Nucl. Mater. 399 (2010) 266–274.
[21] X. Chen, M.A. Sokolov, S. Sham, D.L. Erdman III, J.T. Busby, K. Mo, J.F. Stubbins, J. Nucl. Mater. 432 (2013) 94–101.
[22] K. Mo, H.-M. Tung, X. Chen, Y. Zhao, J. Hansen, J.F. Stubbins, Nucl. Technol. 183 (2013) 455–463.
[23] K. Mo, Microstructural evolution and mechanical behavior in nickel based alloys for very high temperature reactor (Ph.D. thesis), University of Illinois at Urbana-Champaign, 2011.
[24] K. Hrutkay, Evolution of microstructure of Haynes 230 and Inconel 617 under mechanical testing at high temperatures (Master's thesis), 2013.
[25] T.H. Courtney, Mechanical Behavior of Materials, Waveland Press, Long Grove, Illinois, USA, 2005.
[26] M.A. Meyers, K.K. Chawla, Mechanical Behavior of Materials, Cambridge University Press, Cambridge, 2009.
[27] A.K. De, D.C. Murdock, M.C. Mataya, J.G. Speer, D.K. Matlock, Scr. Mater. 50 (2004) 1445–1449.
[28] Y. Miao, K. Mo, Z. Zhou, X. Liu, K.-C. Lan, G. Zhang, M.K. Miller, K.A. Powers, J. Almer, J.F. Stubbins, Mater. Sci. Eng. A 625 (2014) 146–152.
[29] Y. Miao, K. Mo, Z. Zhou, X. Liu, K.-C. Lan, G. Zhang, M.K. Miller, K.A. Powers, Z.-G. Mei, J.-S. Park, et al., Mater. Sci. Eng. A 639 (2015) 585–596.
[30] G. Zhang, K. Mo, Y. Miao, X. Liu, J. Almer, Z. Zhou, J.F. Stubbins, Mater. Sci. Eng. A 637 (2015) 75–81.
[31] K. Mo, Z. Zhou, Y. Miao, D. Yun, H.-M. Tung, G. Zhang, W. Chen, J. Almer, J. F. Stubbins, J. Nucl. Mater. 455 (2014) 376–381.
[32] T. Ungár, I. Dragomir, Á Révész, A. Borbély, J. Appl. Crystallogr. 32 (1999) 992–1002.
[33] T. Ungár, G. Tichy, Phys. Status Solidi A 171 (1999) 425–434.
[34] H. Ledbetter, R.P. Reed, J. Phys. Chem. Ref. Data 2 (1973) 531–618.